

640x486 Long-wavelength Dualband GaAs/AlGaAs Quantum Well Infrared Photodetector (QWIP) Focal Plane Array Camera

S. D. Gunapala, S. V. Bandara, J. K. Liu, S. B. Rafol, E. M. Luong, J. M. Mumolo, and
N. Q. Tran

Center for Space Microelectronics Technology, Jet Propulsion Laboratory
California Institute of Technology, Pasadena, CA 91109

ABSTRACT

An optimized long-wavelength / very long-wavelength two-color Quantum Well Infrared Photodetector (QWIP) device structure has been designed. This device structure was grown on a three-inch semi-insulating GaAs substrate by molecular beam epitaxy (MBE). This wafer was processed into several 640x486 format monolithically integrated 8-9 and 14-15 μm two-color (or dual wavelengths) QWIP focal plane arrays (FPAs). These FPAs were then hybridized to 640x486 silicon CMOS readout multiplexers. A thinned (i.e., substrate removed) FPA hybrid was integrated into a liquid helium cooled dewar for electrical and optical characterization and to demonstrate simultaneous two-color imagery. The 8-9 μm detectors in the FPA have shown background limited performance (BLIP) at 70 K operating temperature, at 300 K background with $f/2$ cold stop. The 14-15 μm detectors of the FPA have reached BLIP at 40 K operating temperature under the same conditions. In this paper we discuss the performance of this long-wavelength dualband QWIP FPA in terms of quantum efficiency, detectivity, noise equivalent temperature difference (NE Δ T), uniformity, and operability.

1. INTRODUCTION

There are many applications that require long-wavelength dualband infrared FPAs. For example, a two-color FPA camera would provide the absolute temperature of a target with unknown emissivity which is extremely important to the process of identifying temperature difference between missile targets, war heads, and decoys. Dualband infrared FPAs can also play many important roles in Earth and planetary remote sensing, astronomy, etc. Furthermore, monolithically integrated dualband FPAs eliminate the beam splitters, filters, moving filter wheels, and rigorous optical alignment requirements imposed on dualband systems based on separate FPAs or a broadband FPA. Dualband FPAs will also reduce the mass, volume, and power requirements of dualband systems. Due to the inherent properties such as narrow-band response, wavelength tailorability, and stability (i.e., low $1/f$ noise) associated with GaAs based QWIPs¹⁻⁵, it is an ideal candidate for large format long-wavelength multi-color FPAs. GaAs based QWIPs will also provide higher uniformity, higher operability, and lower cost as a result of mature GaAs growth and processing technology. In this paper, we discuss the first demonstration of a long-wavelength and very long-wavelength infrared (VLWIR) imaging camera, based on a monolithically integrated 640x486 dualband QWIP FPA.

Until recently, the most developed and discussed two-color QWIP detector was the voltage tunable two stack QWIP. This device structure consists of two connected multi-quantum well (MQW) structures tuned to two different wavelength bands of interest. This device structure utilizes the advantage of electric field domains formation to select the response of one or the other detectors^{6,7} (MQW region). The major disadvantages of this type of two-color QWIP FPA are that, these detector pixels need two different voltages to operate, and the long-wavelength sensitive segment of the device needs very high bias voltage (> 8 V) to turn on the long-wavelength infrared (LWIR) detection. The other disadvantage is that the voltage tunable scheme will not provide simultaneous data from both wavelength bands.

2. DEVICE STRUCTURE

The LWIR and VLWIR dualband QWIP device structure described in this section can be processed into simultaneously readable dualband FPAs with triple contacts to access the CMOS readout multiplexer⁸ or interlace readable dualband FPA (i.e., odd rows for one color and the even rows for the other color). The first approach requires a special dualband readout multiplexer which contains two readout cells per detector unit cell, whereas the second approach needs only an existing single color CMOS readout multiplexer. The advantages of this scheme are that it provides simultaneous data readout and allows the use of currently available single color CMOS readout multiplexers. However, the disadvantage is that it does not provide a full fill factor for both wavelength bands. This problem can be eliminated by fabricating $(n+1)$ terminals (e.g., three terminals for dualband) per pixel and hybridizing with a multicolor readout having n readout cells per detector pitch, where n is the number of bands.

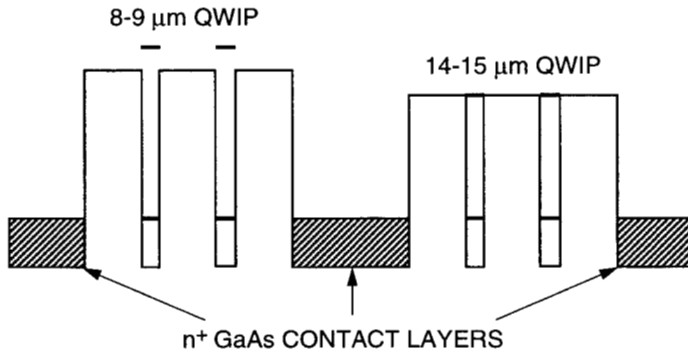


Figure 1. Conduction band energy diagram of the long-wavelength and very long-wavelength two-color infrared detector. The long-wavelength (8-9 μm) sensitive MQW stack utilizes the bound-to-continuum intersubband absorption. The very long-wavelength (14-15 μm) sensitive MQW stack utilizes the bound-to-quasibound intersubband absorption.

The device structure consists of a 30 periods stack, of VLWIR QWIP structure and a second 18 periods stack of LWIR QWIP structure separated by a heavily doped 0.5 μm thick intermediate GaAs contact layer (see Figure 1). The first stack (VLWIR) consists of 30 periods of a 500 \AA $\text{Al}_x\text{Ga}_{1-x}\text{As}$ barrier and a 60 \AA GaAs well. Since the dark current of this device structure is dominated by the longer wavelength portion of the device structure, the VLWIR QWIP structure has been designed to have a bound-to-quasibound intersubband absorption peak at 14.5 μm . The second stack (LWIR) consists of 18 periods of a 500 \AA $\text{Al}_x\text{Ga}_{1-x}\text{As}$ barrier and a narrow 40 \AA GaAs well. This LWIR QWIP structure has been

designed to have a bound-to-continuum intersubband absorption peak at 8.5 μm , since photo current and dark current of the LWIR device structure is relatively small compared to the VLWIR portion of the device structure. This whole dualband QWIP structure is then sandwiched between 0.5 μm GaAs top and bottom contact layers doped with $n = 5 \times 10^{17} \text{ cm}^{-3}$, and has been grown on a semi-insulating GaAs substrate by MBE. Then a 300 \AA $\text{Al}_{0.3}\text{Ga}_{0.7}\text{As}$ stop-etch layer and a 1.0 μm thick GaAs cap layer were grown in situ on top of the device structure. GaAs wells of the LWIR and VLWIR stacks were doped with $n = 6 \times 10^{17}$ and $2.5 \times 10^{17} \text{ cm}^{-3}$ respectively. All contact layers were doped to $n = 5 \times 10^{17} \text{ cm}^{-3}$. The GaAs well doping density of the LWIR stack was intentionally increased by a factor of two to compensate for the reduced number of quantum wells in the LWIR stack. It is worth noting that, the total (dark current + photo current) current of each stack can be independently controlled by carefully designing the position of the upper state, well doping densities, and the number of periods in each MQW stack. All of these features were utilized to obtain approximately equal total currents from each MQW stack. Figure 1 shows the conduction band energy diagram of this dualband QWIP device structure^{9,10}.

Using both selective and non-selective dry etching, this MBE grown device structure was processed into $200 \times 200 \mu\text{m}^2$ test devices. Au/Ge Ohmic contacts were evaporated onto the top, middle, and bottom contact layers. These test detectors were back illuminated through a 45° polished facet as described elsewhere⁵ and simultaneously measured dark current-voltage curves and responsivity spectrums of these vertically integrated dualband QWIPs are shown in Figures 2, 3, and 4. The responsivity of the LWIR detectors peak at 8.4 μm and the peak responsivity (R_p) of the detector is 509 mA/W at bias $V_B = -2 \text{ V}$. The spectral width and the cutoff wavelength of the LWIR detectors are $\Delta\lambda/\lambda = 16\%$ and $\lambda_c = 9.1 \mu\text{m}$ respectively. The responsivity of the VLWIR detectors peak at 14.4 μm and the peak responsivity (R_p) of the detector is 382 mA/W at bias $V_B = -2.0 \text{ V}$. The spectral width and the cutoff wavelength of the VLWIR detector are $\Delta\lambda/\lambda = 10\%$ and $\lambda_c = 15 \mu\text{m}$ respectively. The measured absolute peak responsivity of both LWIR and VLWIR detectors are small, up to about $V_B = -0.5 \text{ V}$. Beyond that, it increases almost linearly with bias in both LWIR and VLWIR detectors reaching $R_p = 0.3$ (at $V_B = -2 \text{ V}$) and 1 A/W (at $V_B = -3 \text{ V}$) respectively. This behavior of responsivity versus bias is typical for bound-to-continuum and bound-to-quasibound QWIPs in LWIR and VLWIR bands respectively. The peak quantum efficiency of LWIR and VLWIR detectors were 6.4% and 11.6% respectively at operating bias $V_B = -2 \text{ V}$ indicated in Figure 4 for a 45° double pass.

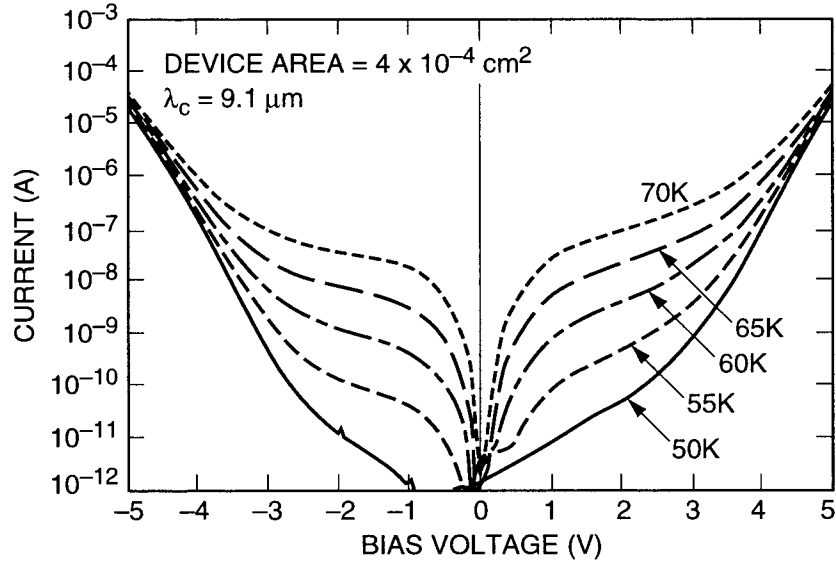


Figure 2. Dark current vs. voltage curves of a LWIR detector at various temperatures. The device area is $4 \times 10^{-4} \text{ cm}^2$.

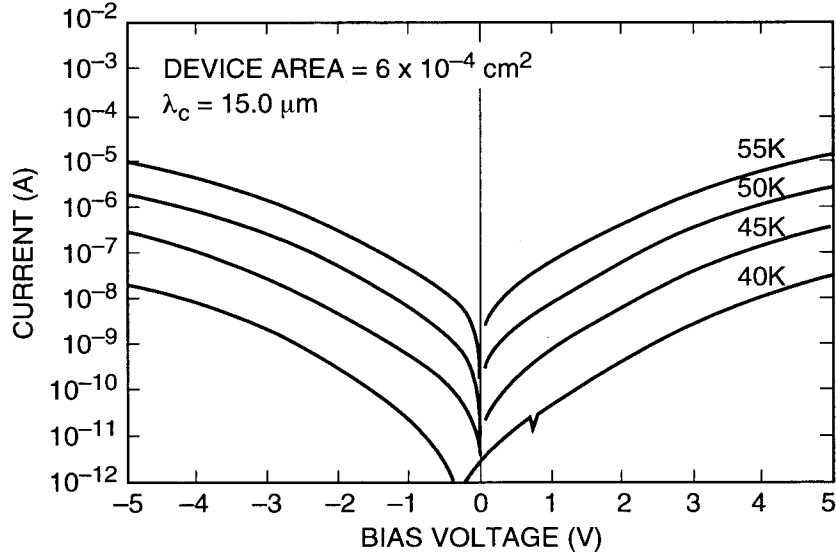


Figure 3. Dark current vs. voltage curves of a VLWIR detector at various temperatures. The device area is $4 \times 10^{-4} \text{ cm}^2$.

The photoconductive gain g was experimentally determined using $g = i_n^2 / 4eI_D B$, where B is the measurement bandwidth, and i_n is the current noise, which was measured using a spectrum analyzer¹¹. The photoconductive gains of the LWIR and VLWIR MQW stacks reached 0.98 and 0.27 respectively at $V_B = -2\text{V}$. The peak detectivity is defined as $D_p^* = R_p \sqrt{AB} / i_n$, where R_p is the peak responsivity, and A is the area of the detector. The areas of the LWIR and VLWIR detectors are 4×10^{-4} and $6 \times 10^{-4} \text{ cm}^2$ respectively. The peak detectivities of both LWIR and VLWIR detectors were estimated at different operating temperatures and bias voltages using experimentally measured noise currents, and results are shown in Figures 5 and 6. Based on single element test detector data, the LWIR detectors show BLIP at bias $V_B = -2 \text{ V}$ and temperature $T = 72 \text{ K}$ for a 300 K background with $f/2$ cold stop. The VLWIR detectors show BLIP under the same operating conditions at 45 K operating temperature.

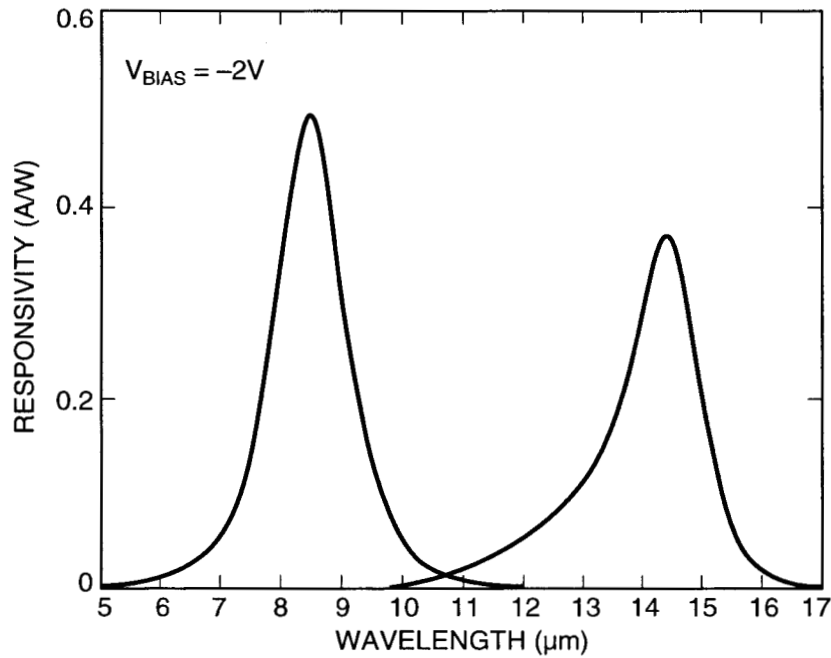


Figure 4. Simultaneously measured responsivity spectrum of vertically integrated LWIR and VLWIR dualband QWIP detector.

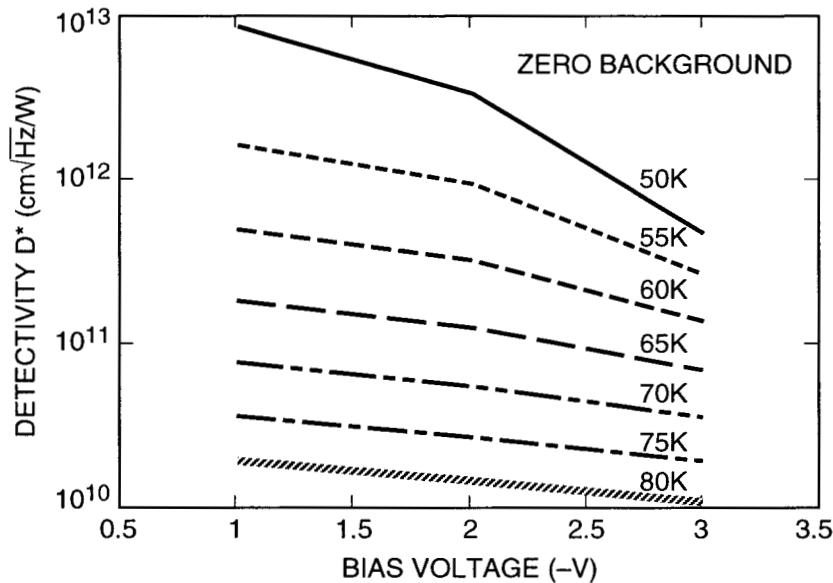


Figure 5. Experimentally measured peak detectivity D^* of LWIR detectors as a function of bias voltage at three different operating temperatures.

3. FOCAL PLANE ARRAYS

It is well known that GaAs/AlGaAs based n-type QWIPs do not absorb infrared radiation incident normal to the surface. Thus, researchers have invented various light coupling schemes such as two-dimensional (2-D) periodic gratings¹², random reflectors¹³, corrugated reflectors¹⁴, lattice mis-match strain material systems, and p-type materials¹⁵. Many of our previous FPAs utilized random reflectors for efficient light coupling. Although random reflectors have achieved relatively high quantum efficiencies with large test device structures, it is not possible to achieve the similar high quantum efficiencies with random reflectors on small FPA pixels due to the reduced width-to-height aspect ratios. In addition, it is difficult to fabricate

random reflectors for shorter wavelength detectors compare to very long-wavelength detectors (i.e., 15 μm) due to the fact that feature sizes of random reflectors are linearly proportional to the peak wavelength of the detectors. For example, the minimum feature size of random reflectors of 15 and 9 μm cutoff FPAs were 1.25 and 0.6 μm respectively. It is difficult to fabricate sub-micron features by contact photolithography. As a result, the random reflectors of the 9 μm cutoff FPA were less sharp and had fewer scattering centers compared to the random reflectors of the 15 μm cutoff QWIP FPA. Thus, 2-D periodic grating structure was used for efficient light coupling into dualband QWIPs. As we have discussed before⁵, two passes of infrared radiation can be coupled to the QWIP detector structure by incorporating a 2-D periodic grating surface¹² on top of the detectors.

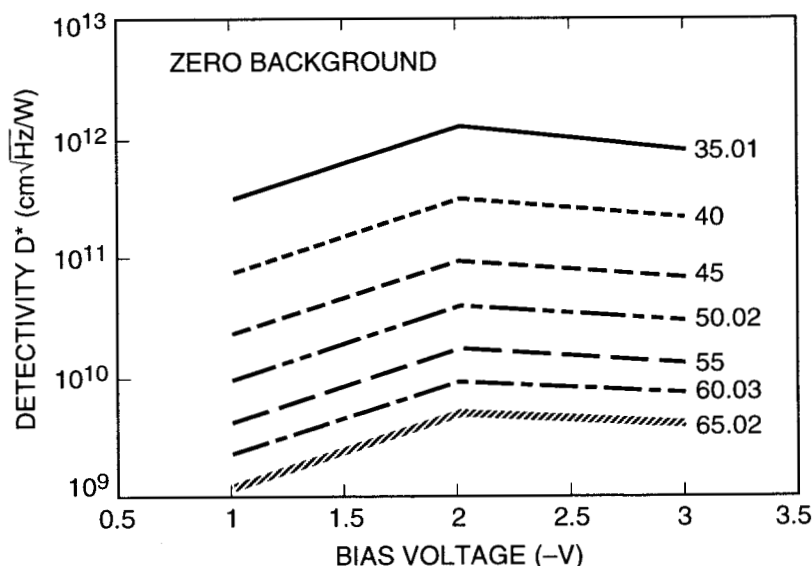


Figure 6. Experimentally measured peak detectivity D^* of a VLWIR detector as a function of bias voltage at three different operating temperatures.

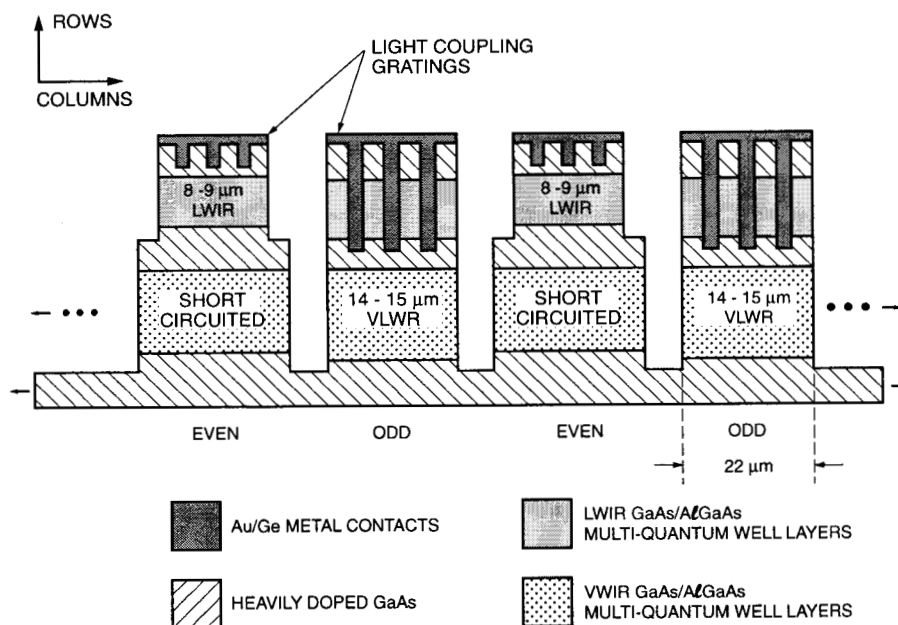


Figure 7. Schematic side view of the interlace dualband FPA. The VLWIR detector pixels in even rows were short circuited at the row-ends. The LWIR detector pixels in odd rows were short circuited by fabricating VLWIR light coupling grating structure through the LWIR portion of detector pixels.

Two different 2-D periodic grating structures were designed to independently couple the 8-9 and 14-15 μm radiation into detector pixels in even and odd rows of the FPAs. The top 0.7 μm thick GaAs cap layer was used to fabricate the light coupling 2-D periodic gratings for 8-9 μm detector pixels. As shown in Figure 7, the light coupling 2-D periodic gratings of the 14-15 μm detector pixels were fabricated through the photosensitive LWIR MQW layers. This grating scheme short circuited all 8-9 μm sensitive detectors in all odd rows of the FPAs. The total thickness of 8-9 μm detector is limited by the grating layer thickness of the VLWIR detector. This 2-D periodic grating structure is fabricated on the detectors by using standard photolithography and $\text{SF}_6:\text{BCl}_3$ selective dry etching.

After the 2-D grating array (calculations of the 2-D grating parameters and light coupling experiments were extensively discussed in reference 12) was defined by the photolithography and dry etching, the LWIR detector pixels of the 640x486 FPAs were fabricated by dry etching through the photosensitive GaAs/ $\text{Al}_x\text{Ga}_{1-x}\text{As}$ MQW layers into the 0.5 μm thick doped GaAs intermediate contact layer. All VLWIR pixels in the even rows of FPAs were short circuited. The VLWIR detector pixels of the FPAs were fabricated by dry etching both MQW stacks into the 0.5 μm thick heavily doped GaAs bottom contact layer. The pitch of the FPA is 25 μm and the actual VLWIR and LWIR pixel sizes are 23x23 and 22x23 μm^2 respectively. The 2-D grating reflectors on top of the detectors were then covered with Au/Ge and Au for Ohmic contact and reflection. Twelve FPAs were processed on a three-inch GaAs wafer. Indium bumps were then evaporated on top of the detectors for silicon readout circuit (ROC) hybridization. Several dualband FPAs were chosen and hybridized (via an indium bump-bonding process) to a 640x486 CMOS multiplexer (Amber AE-181).

The gaps between FPA detectors and the readout multiplexer were backfilled with epoxy. This epoxy backfilling provides the necessary mechanical strength to the detector array and readout hybrid prior to the thinning process. Substrate thinning (or substrate removal) is very important for the success of cryogenic FPA hybrids. During the first step of the thinning process, an approximately 500 μm thick GaAs layer was removed using abrasive polishing or diamond turning. Then Bromine-Methanol chemical polishing was used to remove another approximately 100 μm thick GaAs layer. This step is very important because it removes all scratch marks left on the substrate due to abrasive polishing. Otherwise these scratch marks will be enhanced and propagated into the final step via preferential etching. Then, wet chemical etchant was used to reduce the substrate thickness to several microns and $\text{SF}_6:\text{BCl}_3$ selective dry etching was used as the final etch. This final etching completely removed the remaining GaAs substrate. At this point the remaining GaAs/AlGaAs material contains only the QWIP pixels and a very thin membrane ($\sim 1000\text{\AA}$). The thermal mass of this membrane is insignificant compared to the rest of the hybrid. This allows it to adapt to the thermal expansion and contraction coefficients of the silicon readout multiplexer and completely eliminates the thermal mis-match problem between the silicon based readout and the GaAs based detector array. This basically allows QWIP FPAs to go through an unlimited number of temperature recycles without any indium bump breakage and peeling-off. Furthermore, this substrate removal process provides two additional advantages for QWIP FPAs: the complete elimination of pixel-to-pixel optical cross-talk, and a significant (a factor of two with 2-D periodic gratings) enhancement in optical coupling of infrared radiation into QWIP pixels⁷.

One selected dualband FPA hybrid was mounted onto the cold finger of a liquid helium cooled laboratory test dewar and biased at $V_B = -2\text{V}$. This selected FPA was tested at temperature 40 K. At temperatures below 70 K, the signal-to-noise ratio of the LWIR detector pixels is limited by array non-uniformity, multiplexer readout noise, and photo current noise (for f/2 cold stop). At temperatures above 70 K, temporal noise due to the QWIP's higher dark current becomes the limitation. As mentioned earlier, this higher dark current is due to thermionic emission and thus causes the charge storage capacitors of the readout circuitry to saturate. At temperatures below 40 K, the signal-to-noise ratio of the VLWIR detector pixels are limited by the array non-uniformity, readout multiplexer noise, and photo current noise. Since the QWIP is a high impedance device, it yields a very high charge injection coupling efficiency into the integration capacitor of the multiplexer. The differential resistance R_{Det} of both LWIR and VLWIR pixels at -2 V bias are greater than 7.0×10^{11} Ohms at $T=40$ K and detector capacitance C_{Det} is 3.0×10^{-14} F. The detector dark currents of LWIR and VLWIR detectors are 2.6×10^{-15} and 2.5×10^{-12} A respectively at $T=40$ K. Charge injection efficiency into the CMOS readout multiplexer was calculated as described in reference 2. The calculated charge injection efficiency exceeds 90% at a 30 Hz frame rate. The FPA was back-illuminated through the flat thinned substrate membrane (thickness ≈ 1000 \AA). This FPA gave excellent images with 99.7% of the LWIR pixels and 98% of VLWIR pixels working, demonstrating the high yield of GaAs technology. The operability is defined as the percentage of pixels having noise equivalent differential temperature less than 100 mK at a 300 K blackbody.

4. RESULTS AND DISCUSSION

These dualband FPAs were tested at a background temperature of 300 K, with f/2 cold stop, and at 30 Hz frame rate. Figures 8 and 9 show the measured quantum efficiency of the FPA at an operating temperature of $T = 40$ K, bias $V_B = -2$ V for 300 K

background. The mean value of the long-wavelength FPA quantum efficiency is 12.9% (see Figure 8). This measured value is the integrated FPA quantum efficiency and it includes, the 30% substrate reflection and 85% FPA fill factor. This mean quantum efficiency is a factor of 2.1 higher than the 45° double pass quantum efficiency. This agrees well with the typical 2-D periodic grating light coupling efficiencies seen in other experiments. The uncorrected non-uniformity (i.e., sigma/mean) of the quantum efficiency histogram is 2%. The mean quantum efficiency of 14-15 μm detector pixels in the FPA is 8.9%, and the uncorrected quantum efficiency non-uniformity is about 1%. This mean FPA quantum efficiency value is a factor of 1.3 lower than the 45° test detector quantum efficiency. This shows that the 2-D periodic grating light coupling is very effective in the LWIR region compared to VLWIR region. The integration time used during data acquisition is 3 mSec.

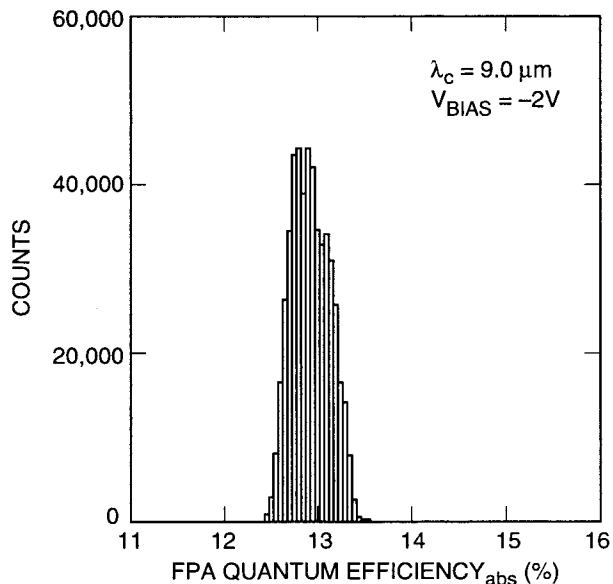


Figure 8. The uncorrected quantum efficiency histogram of 8-9 μm detector pixels of the 640x486 dualband FPA. The mean quantum efficiency is 12.9%. The non-uniformity (i.e., sigma/mean) is 2%.

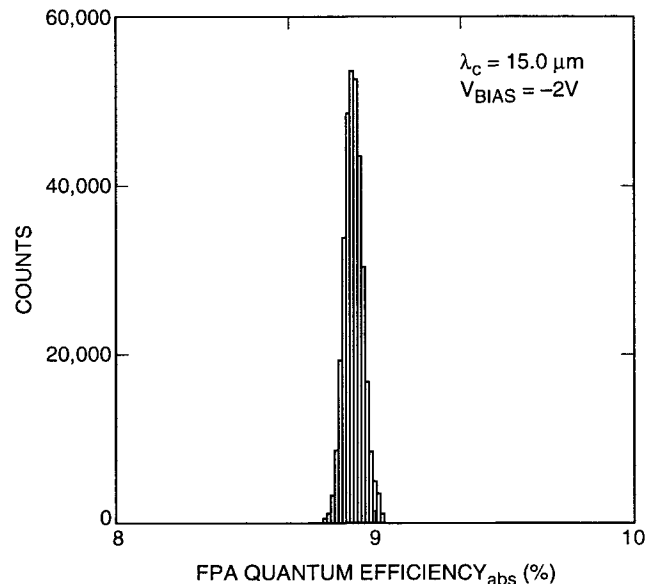


Figure 9. The uncorrected quantum efficiency histogram of 14-15 μm detector pixels of the 640x486 dualband FPA. The mean quantum efficiency is 8.9%. The non-uniformity (i.e., sigma/mean) is 1%.

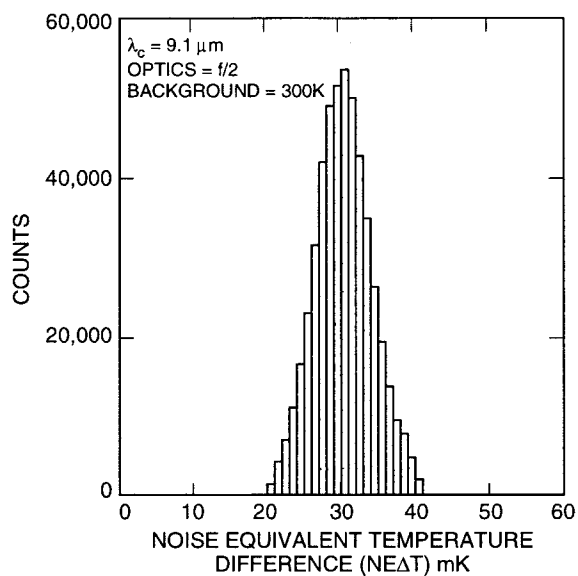


Figure 10. The uncorrected noise equivalent temperature difference (NE Δ T) histogram of 8-9 μm detector pixels of the 640x486 dualband FPA. The mean NE Δ T is 29 mK.

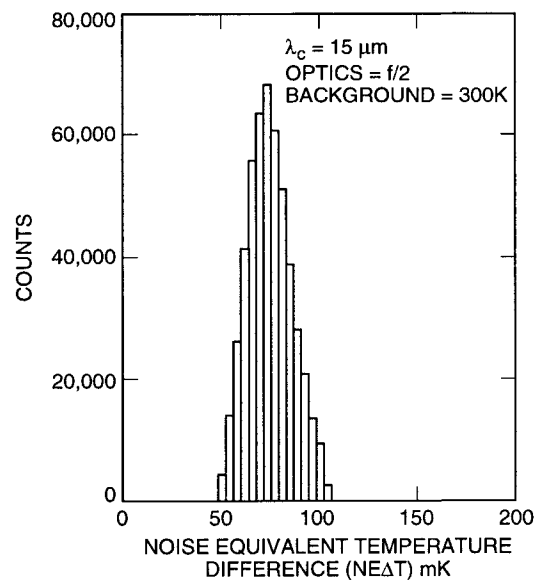


Figure 11. The uncorrected noise equivalent temperature difference (NE Δ T) histogram of 14-15 μm detector pixels of the 640x486 dualband FPA. The mean NE Δ T is 74 mK.

As expected (due to BLIP), the estimated and experimentally obtained NE Δ T values of the LWIR detectors do not change significantly at temperatures below 65 K. The estimated NE Δ T of LWIR and VLWIR detectors at 40 K are 36 and 44 mK respectively. These estimated NE Δ T values based on the test detector data agree reasonably well with the experimentally obtained values. The experimental NE Δ T value is lower than the estimated NE Δ T value of 36 mK. This improvement is attributed to the 2-D periodic grating light coupling efficiency. On the otherhand the experimental VLWIR NE Δ T value is higher than the estimated NE Δ T value of 44 mK. The authors believe this degradation is due to the inefficient light coupling at 14-15 μ m region, readout multiplexer noise, and noise of the proximity electronics. At 40 K the performance of both LWIR and VLWIR detector pixels of this dualband FPA are limited by photo current noise and readout noise.

The uncorrected FPA blackbody detectivity histograms of both LWIR and VLWIR detector pixels are shown in Figures 12 and 13. This detectivity data was also acquired at 300 K background with f/2 cold stop. The mean blackbody detectivity D_{BB}^* values of the LWIR and VLWIR pixels are 2.9×10^{10} and 1.1×10^{10} cm $\sqrt{\text{Hz/W}}$ respectively. This shows that the 8-9 μ m part of this imaging system is 35% BLIP at 300 K background with f/2 cold stop. The 14-15 μ m part of the imaging system reached 15% BLIP at the same operating condition. However, according to theoretical estimates based on single element test detector data, both the LWIR and VLWIR detector pixels should have reached 100% BLIP at 40 K operating temperature. This clearly shows that the performance of this dualband imaging system is limited by the noise of the readout multiplexer and dewar proximity electronics.

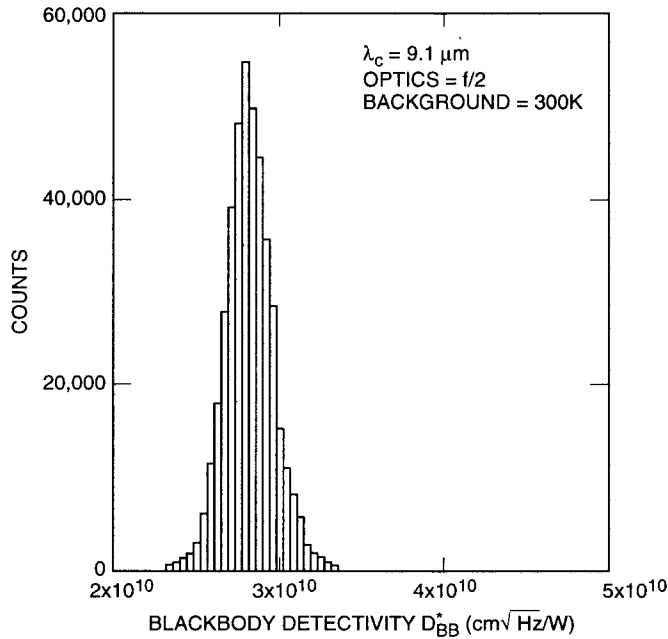


Figure 12. The uncorrected 300 K blackbody detectivity D_{BB}^* histogram of 8-9 μ m detector pixels of the 640x486 dualband FPA. The mean blackbody detectivity D_{BB}^* is 2.9×10^{10} cm $\sqrt{\text{Hz/W}}$.

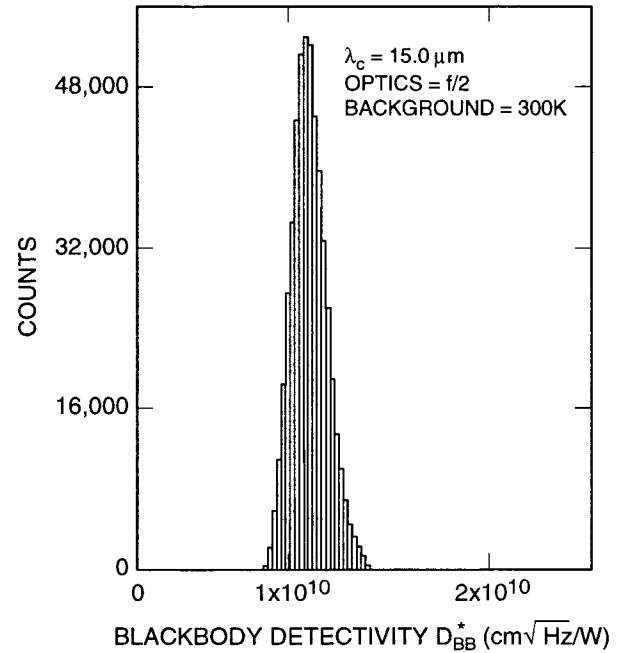


Figure 13. The uncorrected 300 K blackbody detectivity D_{BB}^* histogram of 14-15 μ m detector pixels of the 640x486 dualband FPA. The mean blackbody detectivity D_{BB}^* is 1.1×10^{10} cm $\sqrt{\text{Hz/W}}$.

A dualband FPA hybrid was mounted onto the cold finger of a liquid helium cooled laboratory dewar, to demonstrate simultaneous dualband imagery at 8.5 and 14.5 μ m (shown in Figure 14). The camera is equipped with a 100 mm focal length f/2 germanium lens designed to be transparent in the 8-15 μ m wavelength range, for compatibility with the 8-9 and 14-15 μ m dualband operation. Due to transmission properties of germanium, the 14-15 μ m band has only 30% transmission. This poor optical transmission has really affected the VLWIR performance and image quality. Pixels having NE Δ T > 100 mK are counted as dead pixels. Thus, the operability of 8-9 μ m detector pixels is 99.7% and the operability of 14-15 μ m detector pixels is 98%. However, the actual number of dead pixels (i.e., no photo response) is less than 50, thereby making pixel replacement software unnecessary. It should be noted that this initial FPA is far from optimum and it does not represent the best nonuniformity and operability.



Figure 14. A picture of the 8-9 and 14-15 μm dualband imaging camera.

Video images were taken at a frame rate of 30 Hz, at temperatures as high as $T = 74\text{ K}$, using a ROC capacitor having a charge capacity of 9×10^6 electrons (the maximum number of photoelectrons and dark electrons that can be counted in the time taken to read each detector pixel). Figure 15 shows simultaneously acquired 8-9 and 14-15 micron images using this two-color camera. Figure 16(a) shows a drawing of the filter pattern used to test the operating wavelengths of the two-color camera. The arrow and the semi-circle are open, and transmit all wavelengths. The diamond shape opening is covered with a 10 micron high-pass filter and the rectangle shape is covered with a 10 micron low-pass filter. Figure 16(b) shows a simultaneously acquired image of the object described in the Figure 16(a). This clearly verifies the 8-9 and 14-15 micron two-color operation of this QWIP camera. The readout multiplexer used was a photovoltaic InSb multiplexer which was not optimized to supply the proper bias and impedance levels required by photoconductive QWIPs. Implementation of these improvements should significantly enhance the QWIP FPA operating temperature (i.e., 80 K for 9 μm). In summary, we have demonstrated the first 8-9 and 14-15 μm two-color imaging camera based on a 640x486 dualband QWIP FPA.

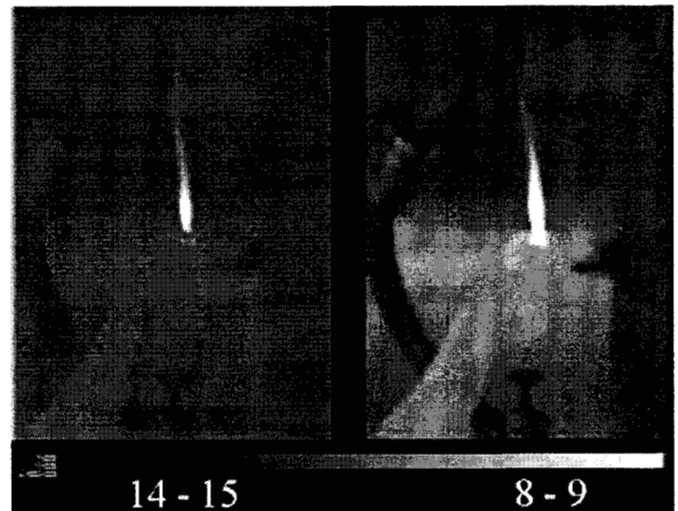
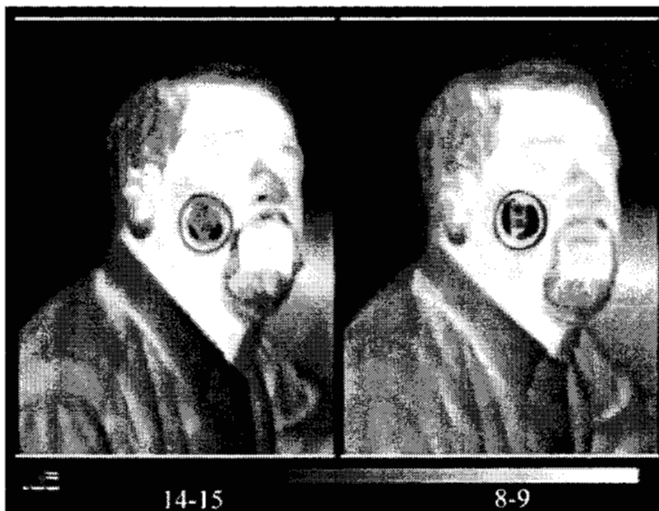


Figure 15. Both pictures show (Flame - simultaneously acquired) two-color images with the 640x486 two-color QWIP camera. Image on the left is from 14-15 micron infrared and the image on the right is from 8-9 micron infrared. Pixel pitch of the FPA is 25 micron. The 14-15 micron image is less sharp due to the diffraction limited spot size being larger than the pixel pitch of the FPA.

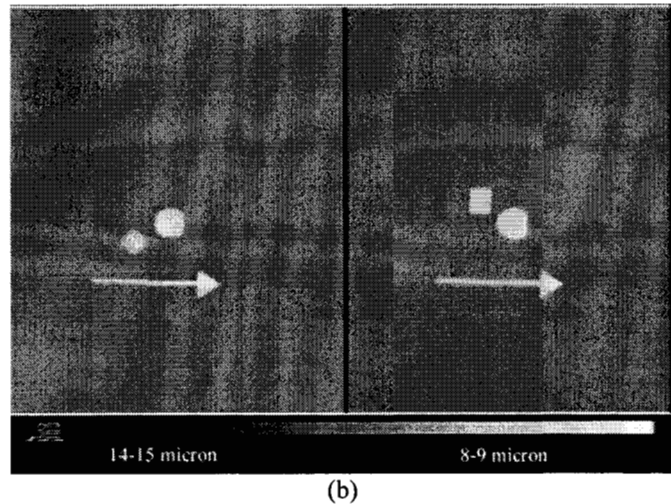
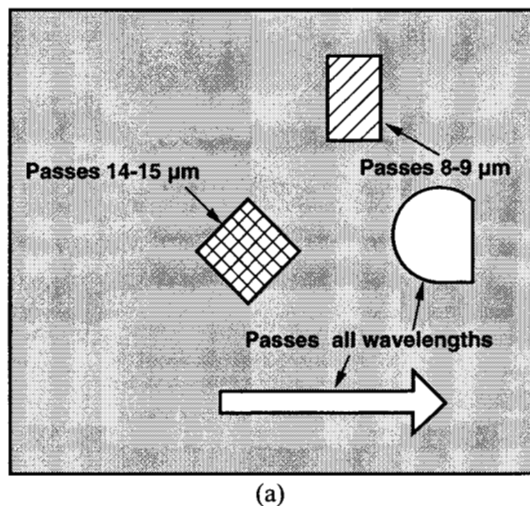


Figure 16. (a) A piece of cardboard with some openings. The arrow and the semi-circle are open, and transmit all wavelengths. The diamond shape opening is covered with a 10 micron high-pass filter and the rectangle shape is covered with a 10 micron low-pass filter. Figure 16(b) shows a simultaneously acquired image of the object described in the Figure 16(a). This clearly verifies the 8-9 and 14-15 micron two-color operation of this QWIP camera.

5. ACKNOWLEDGMENTS

The authors are grateful to Dr. Walt Dyer, and LCDR Chip Buckley of Ballistic Missile Defense Organization for encouragement and support during the work presented in this paper. The research described in this paper was performed by the Center for Space Microelectronics Technology, Jet Propulsion Laboratory, California Institute of Technology, and was jointly sponsored by the Ballistic Missile Defense Organization / Exo-atmospheric Interceptor Technology office, and the Air Force Research Laboratory.

6. REFERENCES

1. S. D. Gunapala, S. V. Bandara, J. K. Liu, W. Hong, M. Sundaram, R. Carralejo, C. A. Shott, P. D. Maker, and R. E. Muller, "Long-wavelength 640x484 GaAs/Al_xGa_{1-x}As Quantum Well Infrared Photodetector Focal Plane Array Camera", SPIE Proceeding, IR Technology and Applications, pp. 722-727, Vol. 3061, 1997.
2. Sarath D. Gunapala, John K. Liu, Jin S. Park, Mani Sundaram, Craig A. Shott, Ted Hoelter, True-Lon Lin, S. T. Massie, Paul D. Maker, Richard E. Muller, and Gabby Sarusi" 9 μm Cutoff 256x256 GaAs/Al_xGa_{1-x}As Quantum Well Infrared Photodetector Hand-Held Camera", IEEE Trans. Electron Devices, **44**, pp. 51-57, 1997.
3. J. Y. Andersson, J. Alverbro, J. Borglind, P. Helander, H. Martijn, and M. Ostlund, "320x240 Pixels Quantum Well Infrared Photodetector (QWIP) Array for Thermal Imaging: Fabrication and Evaluation", SPIE Proceeding, IR Technology and Applications, pp. 740-748, Vol. 3061, 1997.
4. W. A. Beck, T. S. Faska, J. W. Little, J. Albritton, and M. Sensiper, *Proceedings of the Second International Symposium on 2-20 μm Wavelength Infrared Detectors and Arrays: Physics and Applications*, October 10-12, 1994, Miami Beach, Florida.
5. S. D. Gunapala and K. M. S. V. Bandara, *Physics of Thin Films*, Academic Press, **21**, 113 (1995).
6. I. Grave, A. Shakouri, N. Kuze, and A. Yariv, "Control of electric field domain formation in multiquantum well structures", Appl. Phys. Lett. **63**, 1101 (1993).
7. Ting Mei, G. Karunasiri, and S. J. Chua, "Two-color infrared detection using intersubband transitions in multiple step quantum wells with superlattice barriers", Appl. Phys. Lett. **71**, 2017 (1997).

8. S. D. Gunapala, S. V. Bandara, A. Singh, J. K. Liu, E. M. Luong, J. M. Mumolo, and M. J. McKelvey, "Quantum Well Infrared Photodetectors for Low-Background Applications", SPIE Proceeding 3379, 225 (1998).
9. Ph. Bois, E. Costard, J. Y. Duboz, J. Nagle, E. Rosencher, and B. Vinter, "Optimized multi-quantum well infrared detectors ", SPIE Proceeding, Infrared Technology, pp. 755-766, Vol. 2552, 1995.
10. M. Z. Tidrow, J. C. Chiang, Sheng S. Li, and K. Bacher, "A high strain two-stack two-color quantum well infrared photodetector", Appl. Phys. Lett. **70**, 859 (1997).
11. G. Hasnain, B. F. Levine, S. Gunapala, and N. Chand, Appl. Phys. Lett. **57**, 608 (1990).
12. J. Y. Andersson, L. Lundqvist, and Z. F. Paska, Appl. Phys. Lett. **58**, 2264 (1991).
13. G. Sarusi, B. F. Levine, S. J. Pearton, K. M. S. V. Bandara, and R. E. Leibenguth, Appl. Phys. Lett. **64**, 960 (1994).
14. K. K. Choi, A. C. Goldberg, N. C. Das, M. D. Jhabvala, R. B. Bailey, and K. Vural, SPIE **3287**, 118 (1998).
15. S. S. Li and Y. H. Wang, Quantum Well Intersubband Transition Physics and Devices, NATO ASI Series, Kluwer Academic, **270**, 29 (1994).